RSC Advances

PAPER

View Article Online
View Journal | View Issue

Cite this: *RSC Adv.*, 2020, **10**, 34225

Donor–acceptor duality of the transition-metal-like B_2 core in core–shell-like metallo-borospherenes $La_3\&[B_2@B_{17}]^-$ and $La_3\&[B_2@B_{18}]^-$†

Xiao-Yun Zhao,[ab] Miao Yan,[a] Zhihong Wei*[a] and Si-Dian Li *[a]

Transition-metal doping induces dramatic structural changes and leads to earlier planar → tubular → spherical → core–shell-like structural transitions in boron clusters. Inspired by the newly discovered spherical trihedral metallo-borospherene D_{3h} $La_3\&B_{18}^-$ (**1**) (Chen, *et al.*, Nat. Commun., 2020, **11**, 2766) and based on extensive first-principles theory calculations, we predict herein the first and smallest core–shell-like metallo-borospherenes C_{2v} $La_3\&[B_2@B_{17}]^-$ (**2**) and D_{3h} $La_3\&[B_2@B_{18}]^-$ (**3**) which contain a transition-metal-like B_2 core at the cage center with unique donor–acceptor duality in $La_3\&B_n^-$ spherical trihedral shells (n = 17, 18). Detailed energy decomposition and bonding analyses indicate that the B_2 core in these novel complexes serves as a π-donor in the equatorial direction mainly to coordinate three La atoms on the waist and a π/σ-acceptor in the axial direction mainly coordinated by two B_6 triangles on the top and bottom. These highly stable core–shell complexes appear to be spherically aromatic in nature in bonding patterns. The IR, Raman, and photoelectron spectra of **2** and **3** are computationally simulated to facilitate their spectroscopic characterizations.

Received 5th August 2020
Accepted 9th September 2020

DOI: 10.1039/d0ra06769e

rsc.li/rsc-advances

1. Introduction

As a prototypical electron-deficient element, boron exhibits diverse geometrical structures and bonding patterns in both bulk allotropes and polyhedral molecules.[1,2] Persistent joint photoelectron spectroscopy (PES) and first-principles theory investigations in the past two decades have unveiled a rich landscape for size-selected boron nano-clusters ($B_n^{-/0}$) from planar or quasi-planar (2D) structures (n = 3–38, 41–42)[3–8] to cage-like borospherenes (C_3/C_2 B_{39}^- and D_{2d} $B_{40}^{-/0}$) which are all characterized with delocalized multi-centre bonding.[9,10] Seashell-like borospherenes C_2 B_{28}^- and C_s B_{29}^- were later confirmed in PES measurements to be minor isomers of the monoanions.[11,12] The borospherene family has been systematically expanded at first-principles theory level to the cage-like B_n^q series (n = 36–42, $q = n - 40$) in different charge states.[13–16] More complicated structural competitions exist in medium-sized boron clusters, with B_{46} being theoretically predicted to be the smallest core–shell-like boron cluster reported to date, while B_{48}, B_{54}, B_{60}, and B_{62} are proposed to possess bilayer structures.[17,18] Joint ion-mobility experiments and density functional theory (DFT) investigations, on the other hand, indicated that bare B_n^+ boron cluster monocations possess double-ring tubular structures in the size range between n = 16–25.[19]

Transition-metal-doping induces dramatic structural changes and leads to earlier planar → tubular → spherical → core–shell-like structural transitions in boron clusters. Perfect transition-metal-centred 2D boron wheels D_{8h} $Co@B_8^-$, D_{9h} $Ru@B_9^-$, and D_{10h} $Ta@B_{10}^-$, half-sandwich SmB_6^-, PrB_7^-, CoB_{12}^-, and RhB_{12}^-,[20–23] double-ring tubular CoB_{16}^- (ref. 24) and RhB_{18}^-,[25] and perfect inverse sandwich D_{7h} $La_2B_7^-$,[26] D_{8h} $La_2B_8^-$,[27] and D_{9h} $La_2B_9^-$ (ref. 26) have been successively characterized in PES experiments. The first experimentally observed tri-lanthanide-doped inverse triple-decker C_{2v} $La_3B_{14}^-$ (ref. 28) contains two conjoined B_8 rings which share a B_2 unit on the waist. With four more B atoms added in, the first perfect spherical trihedral metallo-borospherene D_{3h} $La_3\&B_{18}^-$ (**1**) with three equivalent deca-coordinate La atoms as integral parts of the cage surface were discovered very recently in a joint PES experimental and theoretical investigation.[29] Exohedral metallo-borospherenes $M\&B_{40}$ (M = Be, Mg)[30] and $Ni_n\&B_{40}$ (n = 1–4)[31] were previously proposed in theory which contain hepta-coordinate metal centres in η^7-B_7 rings on the cage surface of B_{40}. Our group proposed very recently at first-principles theory level the smallest perfect spherical trihedral metallo-borospherenes D_{3h} $Ta_3\&B_{12}^-$ which contains three equivalent octa-coordinate Ta centres as integral parts of the cage surface.[32] However, to the best of our knowledge, there have been no core–shell-like metallo-borospherenes reported to date in either theory or experiments.

[a]*Key Laboratory of Materials for Energy Conversion and Storage of Shanxi Province, Institute of Molecular Science, Shanxi University, Taiyuan 030006, China. E-mail: weizhihong@sxu.edu.cn; lisidian@sxu.edu.cn*

[b]*Department of Applied Chemistry, Yuncheng University, Yuncheng 044000, China*

† Electronic supplementary information (ESI) available. See DOI: 10.1039/d0ra06769e

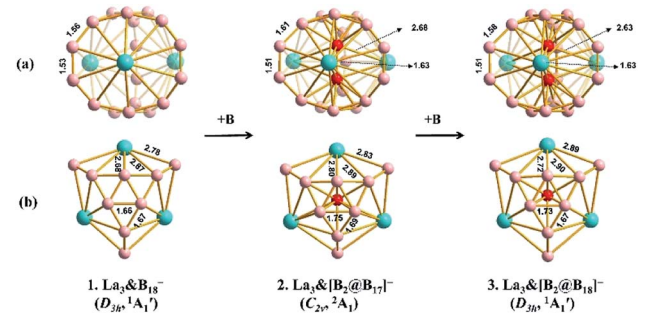

Fig. 1 Side (a) and top (b) views of the global minimum structures of D_{3h} $La_3\&B_{18}^-$ (**1**), C_{2v} $La_3\&[B_2@B_{17}]^-$ (**2**), and D_{3h} $La_3\&[B_2@B_{18}]^-$ (**3**) at PBE0/B6-311+G(d)/La/ECP28MWB level, with the B_2 core highlighted in red and important bond lengths indicated in Å.

Based on extensive global minimum (GM) searches and first-principles theory calculations, we predict herein the first and smallest core–shell-like (CSL) spherical trihedral metallo-borospherenes C_{2v} $La_3\&[B_2@B_{17}]^-$ (**2**) and D_{3h} $La_3\&[B_2@B_{18}]^-$ (**3**) which contain three equivalent La atoms as integral parts of cage surface and, more importantly, a B_2 core with unusual donor–acceptor duality at the cage centre (Fig. 1 and TOC) which exhibits obvious transition-metal-like behaviour. With the formation of effective coordination interactions between B_2 and $La_3@B_n^-$ spherical shells ($n = 17$, 18), the B_2 core plays an essential role in stabilizing these spherically aromatic CSL complexes. $La_3\&[B_2@B_{17}]^-$ (**2**) and $La_3\&[B_2@B_{18}]^-$ (**3**) prove to possess the optimum core–shell combinations to demonstrate the donor–acceptor duality of a B_2 core in $La_3\&B_n^-$ spherical shells ($n = 17$, 18).

2. Theoretical procedure

Extensive global minimum (GM) searches were performed on $B_nLa_3^-$ ($n = 19$ and 20) using the TGmin 2.0 algorithms,[33,34] in conjunction with manual structural constructions. Approximately 2000 trial structures were probed on the potential energy surface for each species in both singlet and triplet states. The low-lying isomers were then fully re-optimized at both the hybrid PBE0 (ref. 35) and TPSSh[36] DFT levels with the 6-311+G(d)[37] basis set for B and Stuttgart relativistic small-core pseudopotential (ECP28MWB) for La[38,39] using the Gaussian 09 program suite (with the self-consistent-field convergence criteria of scf = tight),[40] with vibrational frequencies checked to make sure all the low-lying isomers obtained are true minima of the systems. Relative energies of the five lowest-lying isomers were further refined at the more accurate CCSD(T) level[41–43] at PBE0 geometries using the MOLPRO program,[44] with the same basis sets. Bonding analyses were performed using the adaptive natural density partitioning (AdNDP)[45,46] approach. Born–Oppenheimer molecular dynamics (BOMD) simulations were performed on $La_3\&[B_2@B_{17}]^-$ (**2**) and $La_3\&[B_2@B_{18}]^-$ (**3**) for 30 ps at different temperatures using the CP2K software package[47] with the time step of 10 fs at the PBE/TZVP level, starting from the equilibrium GM geometry with random velocities assigned to the atoms in a cubic box with 15 Å on each side. The initial conditions were chosen to correspond to a microcanonical ensemble with the energy cutoff of 300 eV. The iso-chemical shielding surfaces (ICSSs)[48,49] were generated with the Multiwfn 3.7 code.[50] A detailed energy decomposition analysis with natural orbitals for chemical valence (EDA-NOCV)[51–53] was carried out using the ADF program package[54] at the PBE0/TZP-ZORA level where scalar relativistic effects were considered for the metals using the zeroth-order regular approximation (ZORA).[55–57] The frozen core approximation was not employed in these computations. In the EDA analysis, the interaction energy (ΔE_{int}) between two fragments is decomposed into the electrostatic interaction energy (ΔE_{elstat}), the Pauli repulsion (ΔE_{Pauli}), and the orbital interaction energy (ΔE_{orb}) in eqn (1).

$$\Delta E_{int} = \Delta E_{elstat} + \Delta E_{Pauli} + \Delta E_{orb} \quad (1)$$

3. Results and discussions

We start from closed-shell D_{3h} $La_3\&[B_2@B_{18}]^-$ (**3**, $^1A'_1$), the smallest perfect CSL metallo-borospherene which can be obtained by adding a B_2 core directly inside the experimentally observed $La_3\&B_{18}^-$ (**1**) shell[29] (Fig. 1). Extensive global searches indicate that $La_3\&[B_2@B_{18}]^-$ (**3**) is the well-defined GM of $La_3B_{20}^-$ in thermodynamics in both singlet and triplet states, with the lowest vibrational frequency of $\nu_{min} = 113.2$ cm^{-1} (e′) and large HOMO–LUMO gap of $\Delta E_{gap} = 2.30$ eV at PBE0/B6-311+G(d)/La/ECP28MWB level.[37–39] It lies 0.51, 0.52, 0.29 eV lower than the second lowest-lying triple-decker C_s $La_3\&B_{20}^-$ at PBE0,[35] TPSSh,[36] and CCSD(T)[41–43] levels with the same basis sets, respectively (Fig. S1†). The D_{3h} $La_3\&B_{18}^-$ shell in $La_3\&[B_2@B_{18}]^-$ (**3**) contains three equivalent deca-coordinate La atoms at the centres of three conjoined η^{10}-B_{10} rings which share two B_6 triangles on the top and bottom interconnected by three B_2 units on the waist. All the fifteen lowest-lying isomers within 1.1 eV possess 3D structures in singlet states, with the second, third, and fourth CSL $La_3\&[B_n@B_{20-n}]^-$ isomers ($n = 1$–3) lying 0.65, 0.88, and 1.08 eV higher than the GM at PBE0 level, respectively. Triplet isomers are found to be much less stable than the GM, with the first triplet structure C_s $La_3\&[B_2@B_{18}]^-$ (**14**) possessing the relative energies +0.97 eV at PBE0 (Fig. S1†). Removing one B atom from a B_2 unit on the waist in $La_3\&[B_2@B_{18}]^-$ (**3**) results in the doublet C_{2v} $La_3\&[B_2@B_{17}]^-$ (**2**, $^2A_1$) which, with one η^{10}-B_{10} ring in the front and two equivalent η^9-B_9 rings on the back, is also the GM of the system (Fig. S2†).

Extensive BOMD simulations are performed on $La_3\&[B_2@B_{17}]^-$ (**2**) and $La_3\&[B_2@B_{18}]^-$ (**3**) at 300, 700 and 1000 K to check their dynamical stabilities in gas-phases, respectively (Fig. S3 and S4†). Both of these CSL species appear to be dynamically stable at 1000 K, with the small calculated average root-mean-square-deviations of RMSD = 0.13, 0.14 Å and maximum bond length deviations of MAXD = 0.40, 0.47 Å, respectively. No high-lying isomers were observed during the simulations.

Natural bonding orbital (NBO) analyses[58] show that the three equivalent La centres in $La_3\&[B_2@B_{18}]^-$ (**3**) possess the electronic configuration of La $[Xe]6s^{0.12}5d^{1.46}$, natural atomic

charge of $q_{La} = +1.28|e|$, and total Wiberg bond index of $WBI_{La} = 3.11$, respectively, indicating that each La centre in these complexes donates its $6s^2$ electrons almost completely to the B_{20} ligand, while, in return, accepts about half an electron in its partially filled 5d orbitals from the CSL B_{20} framework (Table S1†). As a commonly used indicator of bond order,[13–16] the calculated B–B Wiberg bond index of $WBI_{B-B} = 0.73$ in the B_2 core indicates the formation of a B–B single bond, the B⋯B bond orders of $WBI_{B-B} = 0.27–0.43$ between the two B_6 triangles and B_2 core suggest the existence of $B_6 \cdots B_2$ coordination interactions in axial direction, while the B⋯La bond order of $WBI_{La \cdots B} = 0.26$ between the B_2 core and three La atoms evidences the formation of $B_2 \cdots La$ coordination interactions on the equator. The B_2 core thus forms effective coordination interactions with the $La_3B_{18}^-$ shell around it, akin to a transition metal centre in traditional complexes.

Detailed EDA-NOCV analyses[51–53] at PBE0/TZP-ZORA level[35,55–57] – with various interacting fragments in different charge states[59] considered (Table S2†) indicate that, with the smallest orbital interaction energy of $\Delta E_{orb} = -717.9$ kcal mol^{-1}, the B_2 and $La_3\&B_{18}^-$ fragments interaction is best suited to describe the bonding scheme of $La_3\&[B_2@B_{18}]^-$ (**3**). Such a scheme is well in line with the experimental observation that a spherical trihedral $La_3B_{18}^-$ cage is highly stable in gas phase.[29] As for the B_2 core, previous theoretical and experimental investigations demonstrated that the isolation of B_2 allotropes with a B≡B triple bond can be achieved in the formula of L→B≡B←L, where L is N-heterocyclic carbene (NHC),[60,61] carbonyl (CO),[62] or boronyl anion (BO^-).[63] The third excited state ($^1\Sigma_g^+$) of B_2 with two electrons excited from $1\sigma_u$ to $1\pi_u$ rather than the ground state ($^3\Sigma_g^-$) with the valence electron configuration of $1\sigma_g^2 1\sigma_u^2 1\pi_u^2$ was proven to have the most suitable electron configuration ($1\sigma_g^2 1\pi_u^4$) to describe the bonding nature of (NHC)→B≡B←(NHC).[64,65] For $La_3\&[B_2@B_{18}]^-$ (**3**), the B_2 core in the third excited state [$^1\Sigma_g^+$] produces a smaller orbital interaction energy (ΔE_{orb}) than that in the ground state [$^3\Sigma_g^-$] by 261.8 kcal mol^{-1}. We thus choose to use B_2 [$^1\Sigma_g^+$] and $La_3B_{18}^-$ [$^1A_1$] fragments as interacting species to demonstrate the bonding scheme of $La_3\&[B_2@B_{18}]^-$ (**3**) in Fig. 2.

The bonding molecular orbitals (MOs) 29e′, 15e″, 22a′$_1$ and 13a″$_2$ which represent coordination bonding between the B_2 core and $La_3B_{18}^-$ shell are connected with the corresponding fragmental orbitals by red lines in Fig. 2, with the orbital compositions listed in Table S3.† The doubly degenerate MOs 29e′ are mainly composed of contributions from the occupied 1e′ of B_2 core with π character and vacant 29e′ of $La_3B_{18}^-$ with π feature. The doubly degenerate 15e″ are a linear combination of the occupied 15e″ of $La_3B_{18}^-$ with π feature and vacant 1e″ of B_2 core with π* antibonding character. The non-degenerate 22a′$_1$ and 13a″$_2$ mainly originate from the occupied 12a″$_2$ and 20a′$_1$ of $La_3B_{18}^-$ with π character and vacant 3a′$_1$ and 2a″$_2$ of B_2 core with σ bonding and σ* antibonding characters, respectively. The non-degenerate 20a′$_1$ originates almost completely from the 2a′ of B_2 which represents the B–B σ single bond in the B_2 core. As detailed in Table 1, EDA analyses clearly demonstrate that the interaction energy ΔE_{int} between the B_2 core and $La_3\&B_{18}^-$ shell in $La_3\&[B_2@B_{18}]^-$ (**3**) consists of Pauli repulsion ΔE_{Pauli}, coulombic attraction ΔE_{elstat}, and orbital interaction ΔE_{orb}, with slightly more covalent contribution (51.2%) than electrostatic contribution (48.8%). The decompositions of the orbital interactions ΔE_{orb} into pairwise contributions between occupied and vacant MOs of the fragments provide quantitative insight into the charge flow. The strongest orbital interaction $\Delta E_{orb(1)}$ (43.9%) arises mainly from [B_2 (π)] → [$La_3B_{18}^-$ ($\pi_{La(s+d)}$)] in which the B_2 core serves as a π-donor in equatorial

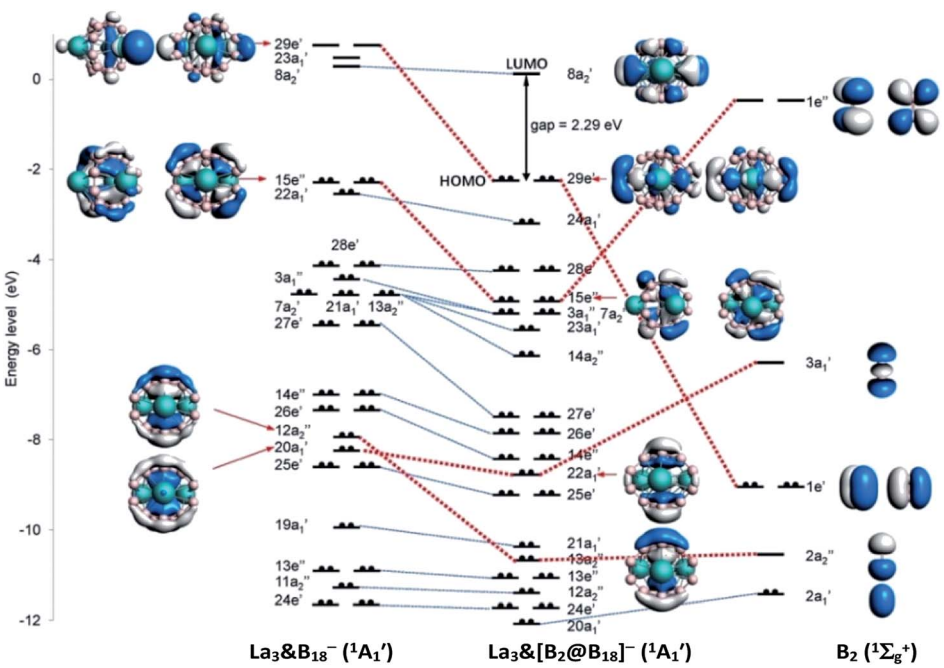

Fig. 2 Bonding scheme of D_{3h} $La_3\&[B_2@B_{18}]^-$ (**3**) using the fragments B_2 ($^1\Sigma_g^+$) and $La_3\&B_{18}^-$ ($^1A_1$) as interacting species at PBE0/TZP-ZORA level.

Table 1 EDA-NOCV analysis of the donor–acceptor interactions of La_3&$[B_2@B_{18}]^-$ (3) at PBE0/TZP-ZORA level using the fragments B_2 [$^1\Sigma_g^+$] and $B_{18}La_3^-$ [$^1A_1$] as interacting species. All energy values are in kcal mol^{-1}

Energy terms	Orbital interaction	B_2 [$^1\Sigma_g^+$] + $B_{18}La_3^-$ [$^1A_1$]
ΔE_{int}		−349.9
ΔE_{Pauli}		1053.5
ΔE_{elstat} [a]		−685.5 (48.8%)
ΔE_{orb} [a]		−717.9 (51.2%)
$\Delta E_{orb(1)}$ [b]	$[B_2\ (\pi)] \rightarrow [La_3B_{18}^-(\pi_{La(s+d)})]$	−315.4 (43.9%)
$\Delta E_{orb(2)}$ [b]	$[B_2\ (\pi^*)] \leftarrow [La_3B_{18}^-\ (\pi_{B(p)})]$	−127.6 (17.8%)
$\Delta E_{orb(3)}$ [b]	$[B_2\ (\sigma_p)] \leftarrow [La_3B_{18}^-\ (\pi_{B(p)})]$	−139.3 (19.4%)
$\Delta E_{orb(4)}$ [b]	$[B_2\ (\sigma_s^*)] \leftarrow [La_3B_{18}^-\ (\pi_{B(p)})]$	−79.1 (11.0%)
$\Delta E_{orb(rest)}$ [b]		−57.2 (7.9%)

[a] The value in parentheses gives the percentage contribution to the total attractive interactions ($\Delta E_{elstat} + \Delta E_{orb}$). [b] The value in parentheses gives the percentage contribution to the total orbital interactions.

direction mainly to coordinate the three La atoms on the waist, while the relatively weaker orbital interaction $\Delta E_{orb(2)}$ (17.8%) originates from $[B_2\ (\pi^*)] \leftarrow [La_3B_{18}^-\ (\pi_{B(p)})]$ where the B_2 core is a π^*-acceptor in axial direction mainly coordinated by two B_6 triangles on the top and bottom. The orbital interactions $\Delta E_{orb(3)}$ (19.4%) and $\Delta E_{orb(4)}$ (11.0%) correspond to $[B_2\ (\sigma_p)] \leftarrow [La_3B_{18}^-\ (\pi_{B(p)})]$ and $[B_2\ (\sigma_s^*)] \leftarrow [La_3B_{18}^-\ (\pi_{B(p)})]$, respectively, in which the B_2 core functions as both σ- and σ*-acceptors in axial direction coordinated mainly by two B_6 triangles on the top and bottom. Fig. S5† further shows the deformation densities $\Delta\rho$ associated with the pairwise interactions $\Delta E_{orb(1)-(4)}$ in La_3&$[B_2@B_{18}]^-$ (3).

Our EDA-NOCV results quantitatively indicate that the B_2 core in the spherically trihedral La_3&$[B_2@B_{18}]^-$ (3) is a considerably strong π-donor to three equivalent La centres in equatorial directions rather than mainly a σ-acceptor in axial direction in the previously reported linear L→B≡B←L complexes.[60–63] The π-donation of the B_2 core effectively weakens the B–B π interactions in the B_2 core and results in a B–B single bond in La_3&$[B_2@B_{18}]^-$ (3) with the B–B bond length of r_{B-B} = 1.63 Å (rather than a B≡B triple bond with the B–B distances of $r_{B\equiv B}$ = 1.45–1.48 Å in L→B≡B←L complexes).[60–63] The π-donation of B_2 core in La_3&$[B_2@B_{18}]^-$ (3) to three equivalent La centers evenly distributed in three equatorial directions is also different from the activation of CO by transition-metal-like NHC→B≡B←NHC in one direction in which an HOMO–LUMO swap occurs in $B_2(NHC)_2$ to form effective electron back-donations with the π* MO of CO.[65] The B_2 unit at the centre serves as both π-donor and σ-acceptor in $B_2(NHC)_2$.[60,61,65]

Detailed adaptive natural density partitioning (AdNDP) bonding analyses[45,46] recover both the localized and delocalized bonds of the concerned complexes. As shown in Fig. 3 in the first row, La_3&$[B_2@B_{18}]^-$ (3) possesses 9 localized 2c–2e σ bonds on three edges on the waist, 8 3c–2e σ bonds on two B_6 triangles on the top and bottom, 1 2c–2e B–B σ bond inside the B_2 core, and 2 7c–2e $B_6(\pi) \rightarrow B(\sigma)$ coordination bonds between the B_2 core and two B_6 triangles on the top and bottom (in which the B_2

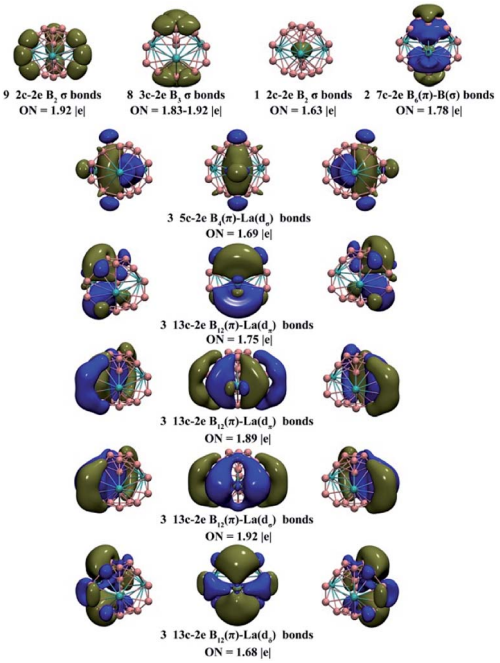

Fig. 3 AdNDP bonding patterns of D_{3h} La_3&$[B_2@B_{18}]^-$ (3) with the occupation numbers (ON) indicated.

core serves as a σ-acceptor). The 3 5c–2e $B_4(\pi)$–$La(d_\sigma)$ bonds in axial direction in the second row mainly represent $B_2 \rightarrow$ La coordination interactions between the B_2 core and three La atoms (in which the B_2 core functions as a π-donor). There exist 3 13c–2e $B_{12}(\pi)$–$La(d_\pi)$ bonds in axis direction in the third row (in which the B_2 core serves as a π*-acceptor), 3 13c–2e $B_{12}(\pi)$–$La(d_\pi)$ bonds in equatorial direction in the fourth row, and 3 13c–2e $B_{12}(\pi)$–$La(d_\sigma)$ bonds in equatorial direction in the fifth row. The nine delocalized (p–d) π interactions evenly distributed on the cage surface form a local 6π-aromatic system over each La&B_{10} pyramidal subunit (similar to the 6π-aromatic system in benzene) and render overall spherical aromaticity to La_3&$[B_2@B_{18}]^-$ (3). The 3 13c–2e (p–d) δ bonds in the sixth row help to further stabilize the CSL complex. As shown in Fig. S6,† a closed-shell C_{2v} La_3&$[B_2@B_{17}]^{2-}$ ($^1A_1$) possesses a similar bonding pattern with La_3&$[B_2@B_{18}]^-$(3). The open-shell C_{2v} La_3&$[B_2@B_{17}]^-$ (2) has the same bonding pattern as La_3&$[B_2@B_{17}]^{2-}$, with the 5c–2e $B_4(\pi)$–$La(d_\sigma)$ bond at the centre in the second row in Fig. S6† singly occupied (which corresponds to its singly occupied HOMO (a_1)).

The spherical aromaticity of La_3&$[B_2@B_{17}]^-$ (2) and La_3&$[B_2@B_{18}]^-$ (3) is further evidenced by their calculated negative nucleus-independent chemical shift (NICS) values[66] of NICS = −80.05 and −80.18 ppm at the cage centres, respectively. Based on the calculated NICS-ZZ components, Fig. S7† plots their isochemical-shielding surfaces (ICSSs)[48,49] with *Z*-axis parallel to the designated C_2 molecular axes of the systems to illuminate the chemical shielding around the La&B_{10} pyramids in these complexes. Obviously, the space inside the spherical trihedron and within about 1.0 Å above the La centres in vertical direction belongs to the chemical shielding region with negative NICS-ZZ values, while the chemical de-shielding areas with positive NICS

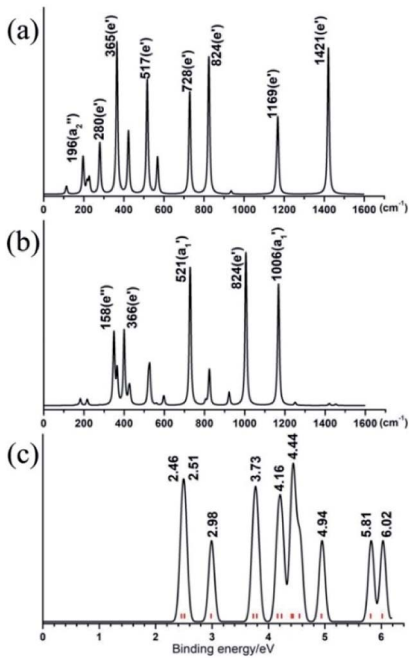

Fig. 4 Simulated (a) IR, (b) Raman and (c) photoelectron spectra of La_3&$[B_2@B_{18}]^-$ (**3**) at PBE0/B6-311+G(d)/La/ECP28MWB level.

values are located outside the B_{10} ring in the horizontal direction. The ICSSs of these complexes in C_2 axial directions appear to be similar to that of the prototypical aromatic benzene C_6H_6 in C_6 axial direction (Fig. S7†).

Finally, we simulate the IR, Raman, and PES spectra of La_3&$[B_2@B_{18}]^-$ (**3**) in Fig. 4 to facilitate its future spectroscopic characterizations in gas-phases. Its major IR bands occur at 365(e′), 517(e′), 728(e′), 824(e′), 1169(e′) and 1421(e′) cm^{-1}, with the corresponding Raman active vibrations located at 158(e″), 366(e′), 521(a'_1), 824(e′) and 1006(a'_1) cm^{-1}, respectively. Detailed vibrational analyses indicate that the symmetrical vibrations at 521(a'_1) cm^{-1} represent typical radial breathing modes (RBMs) of the boron skeleton which can be used to characterize single-walled hollow boron nanostructures.[67] The calculated PES spectrum of La_3&$[B_2@B_{18}]^-$ in Fig. 4c exhibits major spectral features at 2.46, 2.51, 2.98, 3.73–4.94, 5.81 and 6.02 eV, respectively, which correspond to vertical electronic transitions from the ground state of the anion to the ground and excited states of the neutral at the ground-state geometry of the anion. The simulated IR, Raman, and photoelectron spectra of La_3&$[B_2@B_{17}]^-$ (**2**) are depicted in Fig. S8.†

4. Summary

In summary, we have presented in this work a comprehensive first-principles theory investigation on the first and smallest spherically aromatic CSL metallo-borospherenes La_3&$[B_2@B_{17}]^-$ and La_3&$[B_2@B_{18}]^-$ in which the B_2 core and La_3&B_n^- spherical trihedral shells (n = 17 and 18) match both geometrically and electronically. The donor–acceptor duality of the transition-metal-like B_2 core plays an essential role in stabilizing these novel complexes, in particular, its strong π-donation to the three equivalent La atoms in equatorial directions makes major contributions to the overall orbital interaction. Initial results indicate that the experimentally observed spherical trihedral D_{3h} Tb_3&B_{18}^- (ref. 29) can also be used as a cage-like shell to host a B_2 core with donor–acceptor duality. A similar B_2 core in a tubular molecular rotor La_2&$[B_2@B_{18}]^-$ has been reported recently.[68] It is anticipated that more B_n units with donor–acceptor dualities could exist in 3D complexes or low-dimensional nanostructures which may have important applications in materials science, molecular devices, and chemical catalysis.

Conflicts of interest

There are no conflicts to declare.

Acknowledgements

This work was financially supported by the National Natural Science Foundation of China (21720102006 and 21973057 to S.-D. Li). We thank the helpful discussions on EDA-NOCV analysis with Prof. Lili Zhao from Nanjing Tech University and Dr Jun Liu from FermiTech (Beijing) Co. Ltd.

Notes and references

1 F. A. Cotton, G. Wilkinson, C. A. Murillo and M. Bochmann, *Advanced Inorganic Chemistry*, Wiley-Interscience, New York, 6th edn, 1999, p. 1355, ISBN 0-471-19957-5.
2 L. S. Wang, *Int. Rev. Phys. Chem.*, 2016, **35**, 69.
3 H. J. Zhai, A. N. Alexandrova, K. A. Birch, A. I. Boldyrev and L. S. Wang, *Angew. Chem., Int. Ed.*, 2003, **42**, 6004–6008.
4 A. P. Sergeeva, D. Y. Zubarev, H. J. Zhai, A. I. Boldyrev and L. S. Wang, *J. Am. Chem. Soc.*, 2008, **130**, 7244–7246.
5 W. Huang, A. P. Sergeeva, H. J. Zhai, B. B. Averkiev, L. S. Wang and A. I. Boldyrev, *Nat. Chem.*, 2010, **2**, 202–206.
6 Q. Chen, T. T. Chen, H. R. Li, X. Y. Zhao, W. J. Chen, H. J. Zhai, S. D. Li and L. S. Wang, *Nanoscale*, 2019, **11**, 9698.
7 T. Jian, X. N. Chen, S. D. Li, A. I. Boldyrev, J. Li and L. S. Wang, *Chem. Soc. Rev.*, 2019, **48**, 3550.
8 H. Bai, T. T. Chen, Q. Chen, X. Y. Zhao, Y. Y. Zhang, W. J. Chen, W. L. Li, L. F. Cheung, B. Bai, J. Cavanagh, W. Huang, S. D. Li, J. Li and L. S. Wang, *Nanoscale*, 2019, **11**, 23286–23295.
9 H. J. Zhai, Y. F. Zhao, W. L. Li, Q. Chen, H. Bai, H. S. Hu, Z. A. Piazza, W. J. Tian, H. G. Lu, Y. B. Wu, Y. W. Mu, G. F. Wei, Z. P. Liu, J. Li, S. D. Li and L. S. Wang, *Nat. Chem.*, 2014, **6**, 727.
10 Q. Chen, W. L. Li, Y. F. Zhao, S. Y. Zhang, H. S. Hu, H. Bai, H. R. Li, W. J. Tian, H. G. Lu, H. J. Zhai, S. D. Li, J. Li and L. S. Wang, *ACS Nano*, 2015, **9**, 754.
11 Y. J. Wang, Y. F. Zhao, W. L. Li, T. Jian, Q. Chen, X. R. You, T. Ou, X. Y. Zhao, H. J. Zhai, S. D. Li, J. Li and L. S. Wang, *J. Chem. Phys.*, 2016, **144**, 064307.
12 H. R. Li, T. Jian, W. L. Li, C. Q. Miao, Y. J. Wang, Q. Chen, X. M. Luo, K. Wang, H. J. Zhai, S. D. Li and L. S. Wang, *Phys. Chem. Chem. Phys.*, 2016, **18**, 29147.

13 Q. Chen, S. Y. Zhang, H. Bai, W. J. Tian, T. Gao, H. R. Li, C. Q. Miao, Y. W. Mu, H. G. Lu, H. J. Zhai and S. D. Li, *Angew. Chem., Int. Ed.*, 2015, **54**, 8160.
14 Q. Chen, H. R. Li, C. Q. Miao, Y. J. Wang, H. G. Lu, Y. W. Mu, G. M. Ren, H. J. Zhai and S. D. Li, *Phys. Chem. Chem. Phys.*, 2016, **18**, 11610.
15 W. J. Tian, Q. Chen, H. R. Li, M. Yan, Y. W. Mu, H. G. Lu, H. J. Zhai and S. D. Li, *Phys. Chem. Chem. Phys.*, 2016, **18**, 9922.
16 Q. Chen, H. R. Li, W. J. Tian, H. G. Lu, H. J. Zhai and S. D. Li, *Phys. Chem. Chem. Phys.*, 2016, **18**, 14186.
17 L. W. Sai, X. Wu, N. Gao, J. J. Zhao and R. B. King, *Nanoscale*, 2017, **9**, 13905–13909.
18 L. Pei, Y.-Y. Ma, M. Yan, M. Zhang, R.-N. Yuan, Q. Chen, W.-Y. Zan, Y.-W. Mu and S. D. Li, *Eur. J. Inorg. Chem.*, 2020, 3296–3301.
19 E. Oger, N. R. M. Crawford, R. Kelting, P. Weis and M. M. K. R. Ahlrichs, *Angew. Chem., Int. Ed.*, 2007, **46**, 8503.
20 T. R. Galeev, C. Romanescu, W. L. Li, L. S. Wang and A. I. Boldyrev, *Angew. Chem., Int. Ed.*, 2012, **51**, 2101–2105.
21 C. Romanescu, T. R. Galeev, W. L. Li, A. I. Boldyrev and L. S. Wang, *J. Chem. Phys.*, 2013, **138**, 134315.
22 C. Romanescu, T. R. Galeev, W. L. Li, A. I. Boldyrev and L. S. Wang, *Acc. Chem. Res.*, 2013, **46**, 350–358.
23 I. A. Popov, W. L. Li, Z. A. Piazza, A. I. Boldyrev and L. S. Wang, *J. Phys. Chem. A*, 2014, **118**, 8098–8105.
24 I. A. Popov, T. Jian, G. V. Lopez, A. I. Boldyrev and L. S. Wang, *Nat. Commun.*, 2015, **6**, 8654.
25 T. Jian, W. L. Li, X. Chen, T. T. Chen, G. V. Lopez, J. Li and L. S. Wang, *Chem. Sci.*, 2016, **7**, 7020–7027.
26 T. T. Chen, W. L. Li, J. Li and L. S. Wang, *Chem. Sci.*, 2019, **10**, 2534–2542.
27 W. L. Li, T. T. Chen, D. H. Xing, X. Chen, J. Li and L. S. Wang, *PNAS*, 2018, **115**, E6972–E6977.
28 T. T. Chen, W. L. Li, W. J. Chen, J. Li and L. S. Wang, *Chem. Commun.*, 2019, **55**, 7864–7867.
29 T. T. Chen, W. L. Li, W. J. Chen, X. H. Yu, X. R. Dong, J. Li and L. S. Wang, *Nat. Commun.*, 2020, **11**, 2766.
30 H. Bai, Q. Chen, H. J. Zhai and S. D. Li, *Angew. Chem., Int. Ed.*, 2015, **54**, 941.
31 H. R. Li, X. X. Tian, X. M. Luo, M. Yan, Y. W. Mu, H. G. Lu and S. D. Li, *Sci. Rep.*, 2017, **7**, 5701.
32 Y. Zhang, X. Y. Zhao, M. Yan and S. D. Li, *RSC Adv.*, 2020, **10**, 29320.
33 Y. F. Zhao, X. Chen and J. Li, *Nano Res.*, 2017, **10**, 3407–3420.
34 X. Chen, Y. F. Zhao, L. S. Wang and J. Li, *Comput. Theor. Chem.*, 2017, **1107**, 57–65.
35 C. Adamo and V. Barone, *J. Chem. Phys.*, 1999, **110**, 6158.
36 J. Tao, J. P. Perdew, V. N. Staroverov and G. E. Scuseria, *Phys. Rev. Lett.*, 2003, **91**, 146401.
37 R. Krishnan, J. S. Binkley, R. Seeger and J. A. Pople, *J. Chem. Phys.*, 1980, **72**, 650.
38 D. Feller, *J. Comput. Chem.*, 1996, **17**, 1571.
39 L. Schuchardt, B. T. Didier, T. Elsethagen, L. Sun, V. Gurumoorthi, J. Chase, J. Li and T. L. Windus, *J. Chem. Inf. Model.*, 2007, **47**, 1045.
40 M. J. Frisch, *et al.*, *Gaussian 09, Revision D.01*, Gaussian Inc., Wallingford, CT, 2009.
41 J. Čížek, *Adv. Chem. Phys.*, 1969, **14**, 35.
42 G. D. Purvis III and R. J. Bartlett, *J. Chem. Phys.*, 1982, **76**, 1910.
43 K. Raghavachari, G. W. Trucks, J. A. People and M. Head-Gordon, *Chem. Phys. Lett.*, 1989, **157**, 479.
44 H. J. Werner, *et al.*, *Molpro*, version 2012.1.
45 N. V. Tkachenko and A. I. Boldyrev, *Phys. Chem. Chem. Phys.*, 2019, **21**, 9590.
46 T. Lu and F. W. Chen, *J. Comput. Chem.*, 2012, **33**, 580.
47 J. VandeVondele, M. Krack, F. Mohamed, M. Parrinello, T. Chassaing and J. Hutter, *Comput. Phys. Commun.*, 2005, **167**, 103.
48 S. Klod and E. Kleinpeter, *J. Chem. Soc., Perkin Trans. 2*, 2001, 1893.
49 E. Kleinpeter, S. Klod and A. Koch, *J. Mol. Struct.*, 2007, **811**, 45.
50 T. Lu and F. W. Chen, *J. Comput. Chem.*, 2012, **33**, 580.
51 T. Ziegler and A. Rauk, *Theor. Chim. Acta*, 1977, **46**, 1–10.
52 M. P. Mitoraj, A. Michalak and T. Ziegler, *J. Chem. Theory Comput.*, 2009, **5**, 962–975.
53 M. Mitoraj and A. Michalak, *Organometallics*, 2007, **26**, 6576–6580.
54 G. te Velde, F. M. Bickelhaupt, E. J. Baerends, C. Fonseca Guerra, S. J. A. van Gisbergen, J. G. Snijders and T. Ziegler, *J. Comput. Chem.*, 2001, **22**, 931–967.
55 C. Chang, M. Pelissier and P. Durand, *Phys. Scr.*, 1986, **34**, 394–404.
56 J. L. Heully, I. Lindgren, E. Lindroth, S. Lundqvist and A. M. Martensson-Pendrill, *J. Phys. B: At. Mol. Phys.*, 1986, **19**, 2799–2815.
57 E. v. Lenthe, E. J. Baerends and J. G. Snijders, *J. Chem. Phys.*, 1993, **99**, 4597–4610.
58 A. E. Reed, L. A. Curtiss and F. Weinhold, *Chem. Rev.*, 1988, **88**, 899.
59 L. Zhao, S. Pan, M. Zhou and G. Frenking, *Science*, 2019, **365**, eaay5021.
60 G. Frenking and N. Holzmann, *Science*, 2012, **336**, 1394–1395.
61 H. Braunschweig, R. D. Dewhurst, K. Hammond, J. Mies, K. Radacki and A. Vargas, *Science*, 2012, **336**, 1420–1422.
62 M. Zhou, N. Tsumori, Z. Li, K. Fan, L. Andrews and Q. Xu, *J. Am. Chem. Soc.*, 2002, **124**, 12936–12937.
63 S. D. Li, H. J. Zhai and L. S. Wang, *J. Am. Chem. Soc.*, 2008, **130**, 2573–2579.
64 N. Holzmann, M. Hermann and G. Frenking, *Chem. Sci.*, 2015, **6**, 4089–4094.
65 H. Zhang, Z. Cao, W. Wu and Y. Mo, *Angew. Chem., Int. Ed.*, 2018, **57**, 13076–13081.
66 P. v. R. Schleyer and C. Maerker, *J. Am. Chem. Soc.*, 1996, **118**, 6317–6318.
67 D. Ciuparu, R. F. Klie, Y. M. Zhu and L. Pfefferle, *J. Phys. Chem. B*, 2004, **108**, 3967–3699.
68 X. Q. Lu, Q. Chen, X. X. Tian, Y. W. Mu, H. G. Lu and S. D. Li, *Nanoscale*, 2019, **11**, 21311–21316.